

A *CloudSat*–*CALIPSO* View of Cloud and Precipitation Properties across Cold Fronts over the Global Oceans

CATHERINE M. NAUD

Department of Applied Physics and Applied Mathematics, Columbia University, and NASA Goddard Institute for Space Studies, New York, New York

DEREK J. POSSELT

Department of Atmospheric, Oceanic and Space Sciences, University of Michigan, Ann Arbor, Michigan

SUSAN C. VAN DEN HEEVER

Department of Atmospheric Science, Colorado State University, Fort Collins, Colorado

(Manuscript received 16 January 2015, in final form 21 April 2015)

ABSTRACT

The distribution of cloud and precipitation properties across oceanic extratropical cyclone cold fronts is examined using four years of combined *CloudSat* radar and *CALIPSO* lidar retrievals. The global annual mean cloud and precipitation distributions show that low-level clouds are ubiquitous in the postfrontal zone while higher-level cloud frequency and precipitation peak in the warm sector along the surface front. Increases in temperature and moisture within the cold front region are associated with larger high-level but lower mid-/low-level cloud frequencies and precipitation decreases in the cold sector. This behavior seems to be related to a shift from stratiform to convective clouds and precipitation. Stronger ascent in the warm conveyor belt tends to enhance cloudiness and precipitation across the cold front. A strong temperature contrast between the warm and cold sectors also encourages greater post-cold-frontal cloud occurrence. While the seasonal contrasts in environmental temperature, moisture, and ascent strength are enough to explain most of the variations in cloud and precipitation across cold fronts in both hemispheres, they do not fully explain the differences between Northern and Southern Hemisphere cold fronts. These differences are better explained when the impact of the contrast in temperature across the cold front is also considered. In addition, these large-scale parameters do not explain the relatively large frequency in springtime postfrontal precipitation.

1. Introduction

The midlatitudes, where most of the world's population resides, are strongly affected by the passage of extratropical cyclones and their warm and cold fronts, and in particular by the amount of precipitation they might produce (e.g., [Stewart et al. 1998](#); [Kunkel et al. 2012](#)). Insufficient precipitation affects crops and water supply, whereas precipitation extremes can result in havoc and severe loss of life and property. In the context of a warming world, it is still unclear whether extratropical cyclones will become more or less frequent

and/or more or less vigorous. While [Feser et al. \(2015\)](#) find that trends depend on the period studied and report no change in the storm numbers over the last 100 years, [Wang et al. \(2013\)](#) find an increase in cyclone activity over 1951–2010 using the twentieth-century reanalysis, and [Berry et al. \(2011\)](#) report a significant decrease in the frequency of fronts in the North Atlantic over 1989–2009. Looking forward, twenty-first-century projections from the models of phase 5 of CMIP (CMIP5) predict a global decrease in midlatitude fronts ([Catto et al. 2014](#)). These trends have implications not only for precipitation extremes but also for wind intensities (e.g., [Mass and Dotson 2010](#)), snow accumulations (e.g., [Kunkel et al. 2013](#)), and Earth's radiation balance (e.g., [Tselioudis et al. 2000](#)).

Independent of what the storm system trends might be, it is important to know how much cloud and precipitation

Corresponding author address: Catherine Naud, Department of Applied Physics and Applied Mathematics, Columbia University, 2880 Broadway, New York, NY 10025.
E-mail: cn2140@columbia.edu

is associated with these extratropical frontal systems. In the southern oceans they can affect a given region every other day (Naud et al. 2014). Frontal precipitation contributes at least 70% of the total precipitation in the storm-track regions, and cold fronts in particular appear to contribute more than 50% to the total, in particular in the southern oceans (Catto et al. 2012).

To better understand the link between environmental conditions and the amount of clouds and precipitation across cold fronts, we use 4 years of satellite-borne NASA *CloudSat* radar (Stephens et al. 2002) and *CALIPSO* lidar (Winker et al. 2009) products and conditional compositing techniques (e.g., Booth et al. 2013). Compositing techniques have been used for two decades now as a means to climatologically characterize the most salient features of extratropical cyclones. Lau and Crane (1995, 1997) pioneered this technique to explore cloud patterns in midlatitude and tropical storms. More recently, this method was used by Bauer and Del Genio (2006) to evaluate models' ability to represent moisture fields in midlatitude cyclones, while Field and Wood (2007) used this method to explore the impact of moisture and cyclone strength on precipitation in the warm conveyor belt of extratropical cyclones. Others have focused on the dynamical properties of the cyclones themselves (Rudeva and Gulev 2011). *CloudSat* and *CALIPSO* observations of clouds have been used in this framework to get at a three-dimensional view of the extratropical cyclones (Govekar et al. 2011) and of the warm and cold fronts (Naud et al. 2010, 2012; Booth et al. 2013). Here we use these datasets and a cold front-centered compositing approach to first explore the average cloud and precipitation characteristics across cold fronts and then, in line with the work of Field and Wood (2007), examine how they change with changes in moisture, temperature, strength of the cyclone, and contrast in temperature across the fronts. We then use these results to explain some differences evident between seasons and the two hemispheres.

2. Data and methods

Following a battery anomaly, *CloudSat* was switched off and eventually removed from the A-Train in 2011. After about a year hiatus, it was returned to the A-Train in 2012 and now collects data during the daytime only. However, at the time of this study, not all products described and used below were processed post-2011, and so the present extratropical cyclone analysis covers a period of four years, from November 2006 to October 2010. The cold fronts are detected for extratropical cyclones over oceans in the two hemispheres between 30°–60°N and 30°–60°S.

a. The datasets

Cloud-cover vertical profiles were obtained from the combined *CloudSat*–*CALIPSO* geometrical profiling with lidar product (GEOPROF–lidar) data files (Mace et al. 2009), which use cloud detections from both the radar and lidar and provide cloud-base and cloud-top heights of up to six layers between the surface and approximately 20 km. We used these profiles to create a cloud mask that utilizes a fixed vertical grid spacing of 250 m; however, we kept the horizontal spacing as in the original files (i.e., *CloudSat* footprint, or ~1 km).

We also utilized the cloud classification product of Wang et al. (2012), provided in the cloud classification (CLDCLASS)–lidar data files, which combines active observations from the *CloudSat* radar and *CALIPSO* lidar with the Moderate Resolution Imaging Spectroradiometer (MODIS; Salomonson et al. 1989) radiances and other ancillary information to indicate the cloud type of each layer reported in the GEOPROF–lidar data files. The cloud types follow the convention used by surface observers: high clouds (i.e., cirrus, cirrostratus, cirrocumulus; referred to as “cirrus” hereafter), altostratus, altocumulus, stratus, stratocumulus, cumulus (includes both congestus and fair weather types), nimbostratus, and deep convection. Cloud layer types are determined based on the cloud-base height, the presence of rain, the horizontal and vertical cloud extents, and the presence of liquid in the cloud. At the time of this study, the database did not contain files for 2006, so the period examined extended from January 2007 to December 2010. According to the product documentation, full orbits were evaluated visually to ensure the accuracy of the product. There may be issues for the correct classification of low-level clouds in the Arctic region, which should not affect our work as our region of interest is restricted to latitudes within 60°N and 60°S. Stratus clouds may not be detected all the time, as the radar sensitivity is not always sufficient to detect them and the lidar may be attenuated by other clouds aloft (Z. Wang 2014, personal communication).

The precipitation information was obtained from the RAIN-PROFILE data files, which, for each *CloudSat* footprint, include the rain rate at the surface, the rain thermodynamic phase type (i.e., no rain, rain, and mixed/snow), and vertical profiles of liquid water content in precipitation and cloud (Lebsock and L'Ecuyer 2011). Lebsock et al. (2011) reported issues caused by saturation in heavy rain events, which means that the rain rate at the surface might be underestimated in these events, and the profiles of liquid water content are not available (i.e., our averages may be biased toward medium and low rain-rate events). Additionally, because of

the strong surface return in the radar profiles, profiles of liquid water content are not provided in the first few bins above the surface. For the same time period, we also extracted the flag that distinguishes between stratiform, convective, and shallow precipitation from the PRECIP-COLUMN data files (Haynes et al. 2009). This flag is obtained based on the altitude at the top of the liquid precipitation layer. All of the datasets utilized are provided along the *CloudSat* orbits with the same horizontal resolution as the *CloudSat* footprint (~ 1 km) and, when appropriate, were regridded vertically to match the same 250-m vertical resolution.

Additionally, we used 6-hourly $0.5^\circ \times 0.667^\circ$ outputs from the NASA Modern-Era Retrospective Analysis for Research and Applications (MERRA; Rienecker et al. 2011), including the temperature, wind, vertical velocity, geopotential height profiles, and the column-integrated precipitable water. These outputs were utilized to both detect the cold fronts and characterize the large-scale conditions and storm characteristics.

b. Compositing method

MERRA temperature, surface winds, and geopotential heights were first used to detect cold fronts. For this, we used a method introduced by Hewson (1998) that isolates fronts based on a series of tests to identify discontinuities of a temperature field. Here we used the potential temperature field at 1 km above the surface (Hewson and Titley 2010). Warm and cold fronts were distinguished by using the geostrophic thermal advection, which is negative along cold fronts. Because we could not differentiate cold and occluded fronts objectively, occluded fronts may be included in our database. As demonstrated by Schemm et al. (2015), this method works best in situations of high baroclinicity. Therefore, to include situations of low baroclinicity to ensure a wider range of dynamical conditions, we also applied a method introduced by Simmonds et al. (2012), which Schemm et al. (2015) found to be more successful in these situations. Simmonds et al. (2012) proposed to use the change in the meridional surface and 850-hPa winds in terms of direction and strength when a cold front travels through a grid cell between two time intervals (6 h). The change in direction should be from the equator toward the poles, and the magnitude should increase by at least 2 m s^{-1} . This method is designed to track mobile fronts (so excludes stationary fronts) and effectively detects mostly cold fronts (Schemm et al. 2015; Rudeva and Simmonds 2015). Where the two methods agreed that a cold front was present, we combined the grid cells that were flagged by each method into a cluster (a cluster contains neighboring cells, allowing a diagonal point of contact). For each cluster

detected by one or both methods, we then applied a method similar to Simmonds et al. (2012) to isolate the frontal boundary by keeping only the easternmost points of the cluster and by applying a smoothing function along the latitude points. Automated front detection is notoriously difficult over regions of varying topography, but here we are only using detections over oceans. The method was evaluated by visual examination of a large collection of individual cases using sea level pressure and potential temperature contour maps as a reference. In addition, density maps of cold front locations were produced and compared to those shown by Schemm et al. (2015), and they were found to be consistent. Frontal detections in the context of operational forecasting are known to be difficult, and forecasters often disagree (Mass 1991). However, in the context of a climatology, automated methods, and these two in particular, have been quite successful since misdetections and mislocations can be acceptable as long as they are not systematic. The Hewson (1998) and Simmonds et al. (2012) methods have both already been tested and used in such climatological studies (Berry et al. 2011; Catto et al. 2012; Catto and Pfahl 2013; Schemm et al. 2015; Rudeva and Simmonds 2015).

To ensure that the cold fronts are related to an extratropical cyclone, we used the Modeling, Analysis, and Prediction (MAP) Program Climatology of Midlatitude Storminess (MCMS) database (<http://gcss-dime.giss.nasa.gov/mcms/>; Bauer and Del Genio 2006), which provides the location and time of a low pressure center every 6 h. The MCMS database is based on ERA-Interim sea level pressures (Dee et al. 2011). For each cold front found over the oceans in the MERRA outputs between November 2006 and October 2010, we searched the MCMS database to find which low pressure center was the closest. Additional considerations were applied in the allocation procedure: the cold front should be, even if only partly, on the equator side of the low pressure center, and the median latitude along the front should be no farther than 15° from the low pressure center to avoid erroneous attribution to another neighboring cyclone (e.g., Bauer and Del Genio 2006).

CloudSat orbits were then selected when they occurred within ± 3 h (the start time of a given orbit may be up to 4.5 h anterior to the cyclone detection) and contained profiles within 25° of the low pressure center. Additionally, profiles were kept only if they were found at least 500 km away from the low pressure center (to avoid contamination by wraparound and warm frontal clouds) but within 10° from any point along the cold front.

Once the appropriate segments of the orbit were isolated, individual profiles from the GEOPROF-lidar, CLDCLASS-lidar, and RAIN-PROFILE data files along

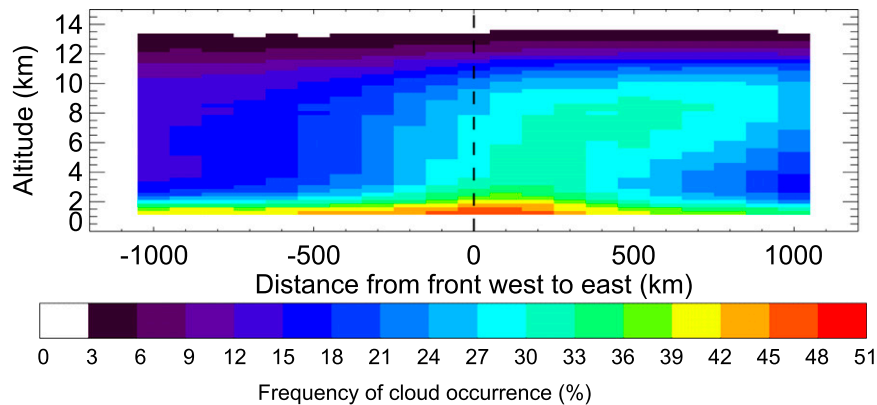


FIG. 1. Frequency of cloud occurrence across cold fronts in the midlatitudes (30° – 60° N and 30° – 60° S) from November 2006 to October 2010 obtained with *CloudSat*–*CALIPSO* GEOPROF–lidar retrievals. The vertical dashed line indicates the location of the surface front.

these segments were collected to populate a vertical transect grid of 250-m vertical resolution from 0 to 15 km and 100-km horizontal resolution from -1000 to 1000 km. The x axis represents the distance from the surface cold front and the y axis the altitude from the surface. This composite grid represents a transect perpendicular to and centered on the front: each observed profile was assigned to a column based on the shortest distance between this profile and any point along the cold front. This compositing technique does not assume a general direction of the cold fronts and averages together information anywhere along and across the cold front.

The frequency of cloud occurrence, of cloud type occurrence, and of rain or snow/mixed precipitation at the surface as well as average liquid water content of precipitation and clouds were then calculated for the entire period, initially regardless of season and hemisphere and then separately for each hemisphere and season. The seasons were defined as December–January–February (DJF), March–April–May (MAM), June–July–August (JJA), and September–October–November (SON).

This method is distinct from the one described in Naud et al. (2010), where *CloudSat* orbits were kept only if they intersected the cold front. Here a given cold front may contribute only a few profiles in our composite grid, as we considered all orbits that occurred in the immediate vicinity, whether they intersected the front or not. This allowed for a greater number of samples and more robust statistics. For the 48 months studied here, the cloud and precipitation composites were constructed using more than 30 000 cold fronts globally (for cyclone centers over oceans between 30° – 60° N and 30° – 60° S) and included at least 400 000 *CloudSat*–*CALIPSO* profiles per 100-km bin.

3. Cloud and precipitation across cold fronts: Global climatology

Figure 1 demonstrates the frequency of occurrence in both hemispheres for all cloud types and all seasons. Focusing first on the western side of the surface front, a relative maximum of 30%–40% frequency of cloud occurrence (regardless of cloud type) is evident within 3 km above the surface and increases from west to east. The frequency of cloud occurrence then decreases from 3 km upward, with high-level clouds occurring less than 15% of the time. In the region of the surface front location, low-level clouds occur up to 50% of the time, while mid- and high-level clouds occur around 30% of the time. On the eastern side of the cold front, low-level clouds again dominate; however, the occurrence of mid- and high-level clouds reaches its maximum within 500 km east of the surface front, and a relative maximum in frequency of occurrence extends upward and eastward up to 1000 km east of the front at 10 km above the surface. The overall shape of the distribution shares some similarities with the classic picture first proposed by Bjerknes and Solberg (1922, their Fig. 1). However, it is better described based on the more recent work of Hobbs (1978, and references therein) or Browning (1986). In particular, consistent with the conceptual model of the warm conveyor belt, the mid- and high-level clouds tend to occur on average to the east of the front (Browning 1986). Figure 1 is a refinement of earlier attempts at compositing GEOPROF–lidar cloud profiles (Naud et al. 2010, their Fig. 14), through utilization of an improved cold front detection algorithm and the inclusion of more profiles. To test the robustness of the composites, in particular their dependency on the number of cold fronts and profiles included, as well as the accuracy of the cold front location with respect to the

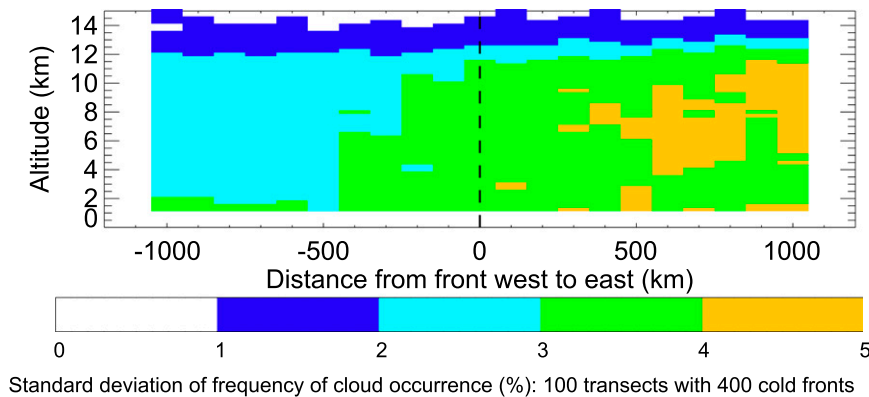


FIG. 2. Standard deviation of frequency of cloud occurrence across the cold fronts obtained for 100 composited transects that include 400 randomly selected cold fronts. The vertical dashed line indicates the location of the surface front.

CloudSat orbit, we randomly drew two independent sets of 400 cold fronts and calculated the frequency of cloud occurrence across the cold fronts with these two subsets. We repeated the operation 50 times, drawing each time from the entire data pool (the 50 pairs are thus not independent), and calculated the standard deviation for all 100 composites. Figure 2 shows the standard deviation of the frequency of cloud occurrence across the cold fronts and reveals that the variability is largest on the eastern side of the surface front but overall never exceeds 5%.

Next, using the cloud classification product, we explore the cloud types that occur across the cold fronts. Figure 3 shows the frequency of occurrence of each cloud type wherever clouds are occurring; that is, the frequency is the number of times a given type occurs divided by the number of times a cloud occurs. Therefore, if only one cloud type exists in a region, the frequency is 100%. In the first 3 km above the surface, on the western side of the cold front, stratocumulus clouds occur most frequently, followed by nimbostratus and cumulus clouds, while on the eastern side, both nimbostratus and stratocumulus clouds occur frequently. Between 3 and 6 km, on the western side of the cold front, altostratus clouds dominate the uppermost part of the altitude range, while nimbostratus clouds dominate the lower altitudes. Cumulus and altocumulus clouds also occur but much less often. On the eastern side of the front, nimbostratus clouds also dominate the lowest levels while altostratus clouds dominate the upper levels. We note that deep convection is detected only 5%–10% of the time, within 300 km to the east of the surface front, and tends to compete with the occurrence of altocumulus and altostratus clouds; that is, there is a slight decrease in frequency of occurrence of these other cloud types where convection occurs. At altitudes above 6 km, altostratus

and cirrus clouds dominate, with the latter type dominating the altitudes above 12 km, with slightly lower frequency of occurrence where deep convection is occurring in the 200-km band to the east of the front. Stratus clouds occur very rarely in these regions, possibly because of the detection issues noted earlier.

The cloud types that exhibit the largest west–east contrast in their frequency of occurrence are cumulus, deep convective, and nimbostratus clouds. Cumulus clouds have been shown to be prevalent west of the cold front, a region characterized by strong surface sensible and latent heat fluxes and cold air in the lower to middle free troposphere coupled with synoptic subsidence. The presence of deep convection along the cold front is consistent with the decreased static stability in the warm sector east of the cold front, coupled with the presence of frontogenetic circulations. The concentration of nimbostratus clouds east of the cold front is in close proximity to the region where convection occurs.

We assessed our statistical approach in a manner similar to that for the cloud frequency of occurrence. We used the random subsets of cold fronts to explore the variability in the frequency of occurrence of each cloud type. For this we calculated the standard deviation across 100 composites comprising 400 cold fronts each (Fig. 4). We found that the variability is greatest where the frequency of occurrence of each cloud type is greatest and only exceeds 10% for the cirrus and stratocumulus types in areas where they make up at least 50% of the clouds.

The precipitation at the surface (Fig. 5) shows variations consistent with the cloud frequency of occurrence. The mean rain rate (which includes periods when it does not rain and clear-sky profiles) reaches its maximum in the first 200 km on the eastern side of the surface front, with greater rates in the eastern than western sectors

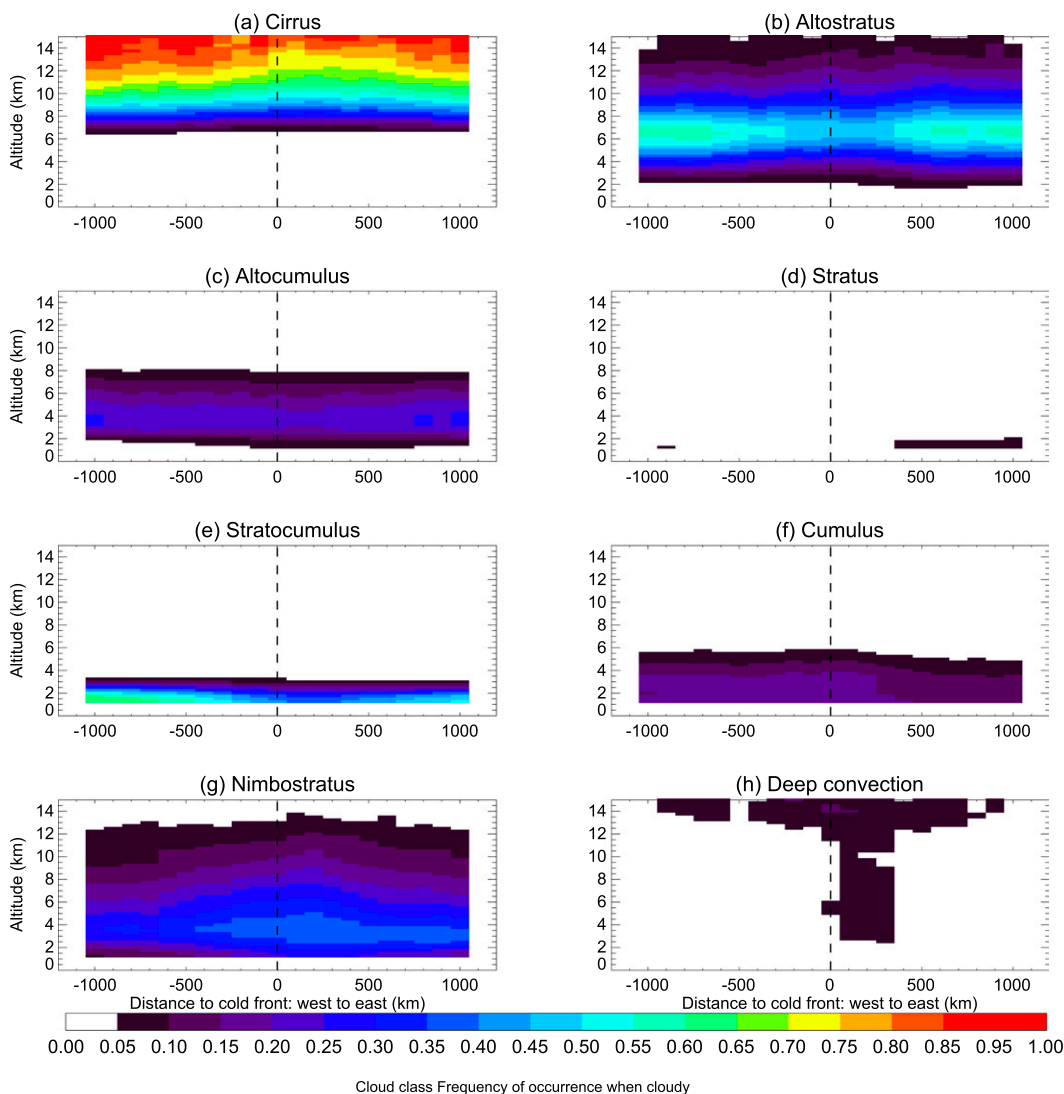


FIG. 3. Frequency of cloud type occurrence when cloudy across cold fronts in the midlatitudes (30° – 60° N and 30° – 60° S) from January 2007 to December 2010 obtained with *CloudSat*–*CALIPSO* CLDCLASS–lidar retrievals. The vertical dashed line indicates the location of the surface front.

(Fig. 5a). The cross-front variations in rain rate trace, almost perfectly, the frequency of nimbostratus occurrence (Fig. 3g). The mean rain rate when raining (Fig. 5b) exhibits spatial variation similar to the overall rain rate, suggesting that when rain occurs it is stronger in the eastern than western side of the cold front. This is more or less corroborated by the frequency of occurrence of rain (Fig. 5c), which shows a very small increase at the surface front into the eastern side (approximately 4%), while the snow/mixed precipitation is more or less constant at about 8% on the western side and decreases, not surprisingly, on the eastern side of the front. Finally, we estimated the fraction of liquid clouds that precipitate by using the profiles of liquid water

content in clouds to flag the presence of a liquid cloud and then count how often these liquid clouds actually precipitate. The fraction of liquid clouds that precipitate (Fig. 5d) is more or less uniform, reaching close to 25% on the western side of the front and steadily increasing eastward of the cold front to 35% at 1000 km. The standard deviations obtained from the 100 subsets mentioned above are included in Figs. 5a–d. These indicate a relatively large variability in the frequency of occurrence of rain and snow/mixed precipitation as well as in the percentage of liquid clouds that rain.

The liquid water content profiles in precipitation and clouds are also averaged along vertical transects across the cold fronts. Figure 6 shows the averages performed

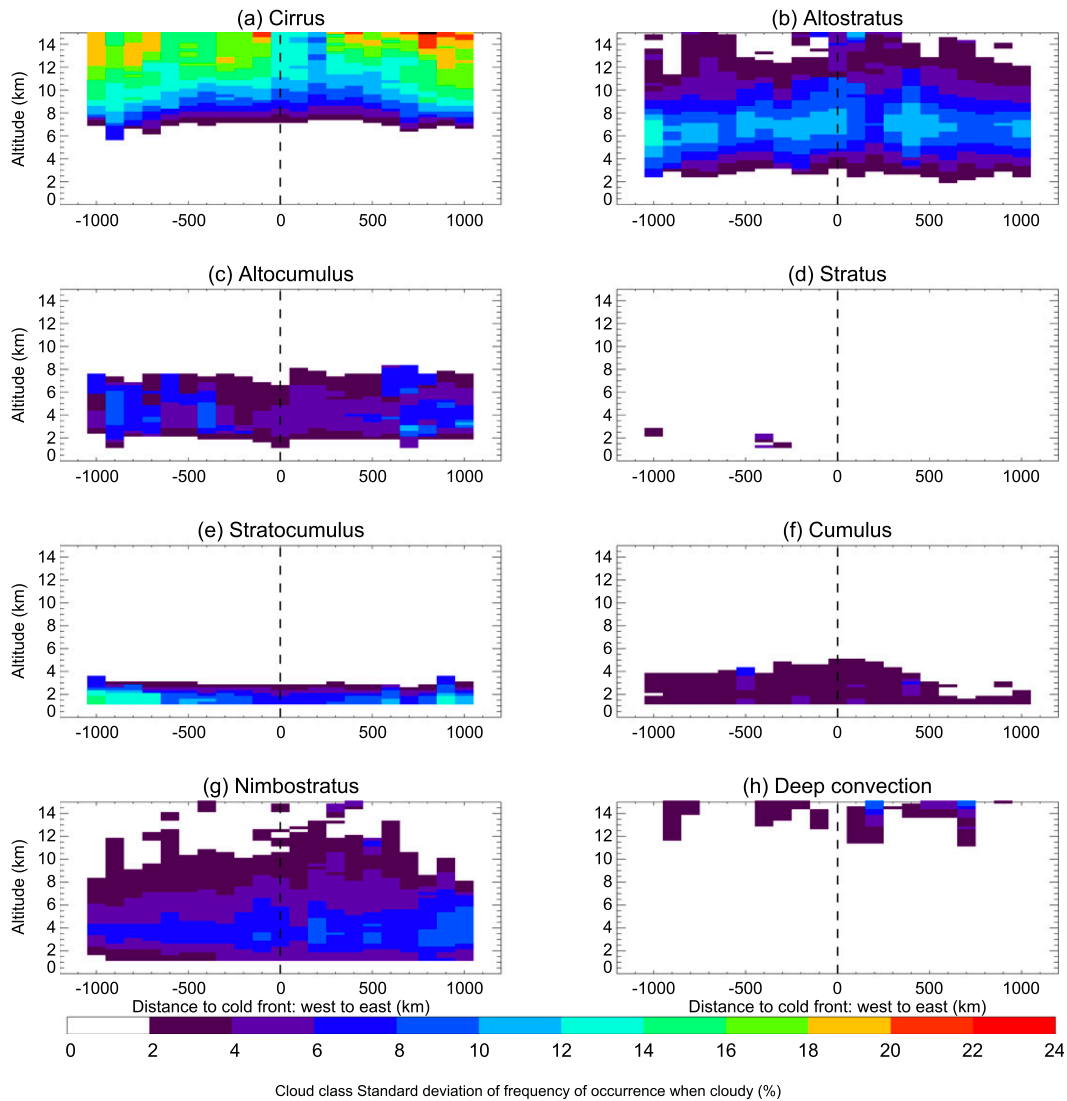


FIG. 4. Standard deviation of the frequency of occurrence of each cloud type across cold fronts where cloudy. The vertical dashed line indicates the location of the surface front.

using only cloudy/precipitating pixels (no clear pixels). Figure 6a shows the mean transect of precipitation liquid water content and indicates that liquid water content in precipitation is a maximum at, and slightly to the east of, the cold front, with values of up to 0.14 g m^{-3} and mostly confined to the lowest 4 km. Water contents are largest where rain rates peak and their variations match the occurrence of nimbostratus clouds. Liquid is also detected between 4 and 10 km, although in smaller quantities. Figure 6c shows the cold front-centered composites of the precipitation-type frequency extracted from the PRECIP-COLUMN data files, which are determined based on the altitude at the top of the liquid precipitation layer (i.e., shallow, stratiform, and convective). The figure shows a dominance of stratiform

precipitation across the entire region, with a slight increase that is accompanied by a decrease in the frequency of shallow and convective precipitation to the east of the surface front. Therefore, to the east of the cold front, liquid above 4 km can probably be attributed to warmer temperatures that lift the melting layer as well as to the presence of convection. To the west of the cold front, this probably reflects the occasional occurrence of convection, presumably when cumulus fields are formed in cold air outbreak conditions. Figure 7a shows the variability in precipitating liquid water content and indicates that above 4 km the variability is large. Cloud liquid water content (Fig. 6b) is a maximum 500–1000 km west of the cold front, below 1 km, in the region of maximum occurrence of stratocumulus clouds;

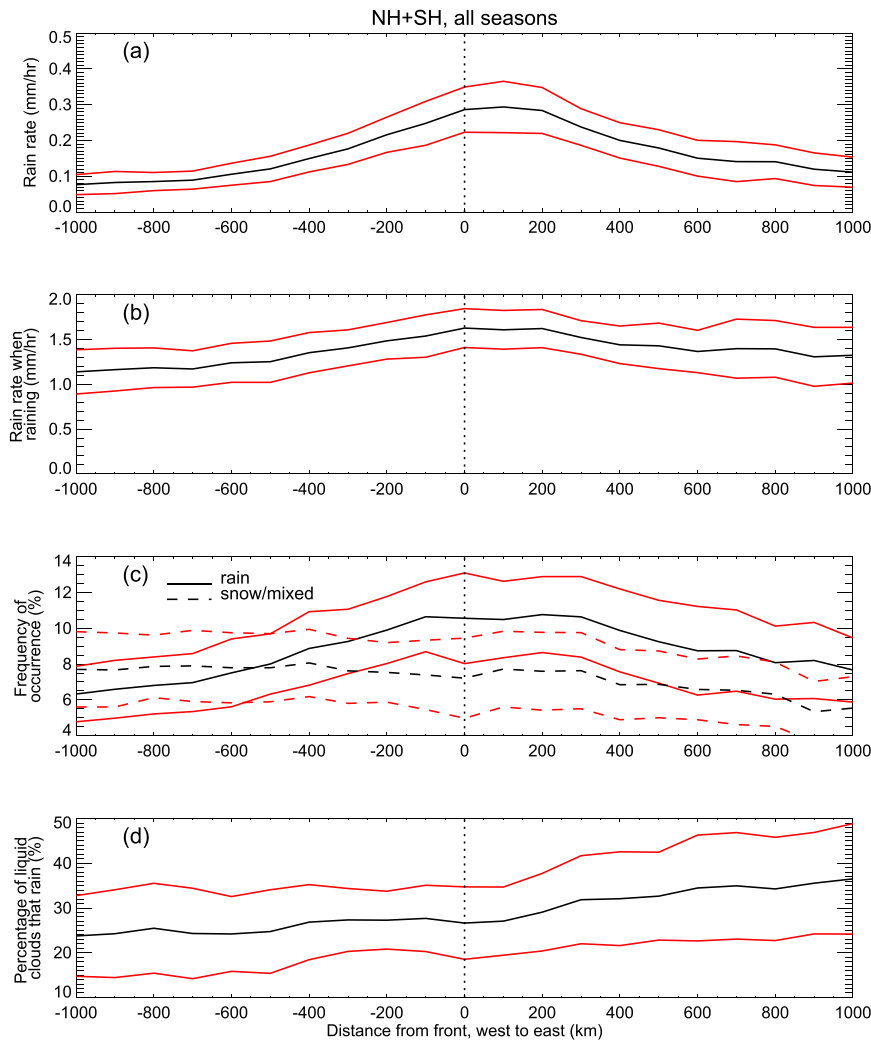


FIG. 5. Midlatitudes (30° – 60° N and 30° – 60° S) composites across cold fronts of (a) rain rates for all profiles, (b) rain rates for raining profiles, (c) frequency of occurrence of rain and snow/mixed precipitation, and (d) percentage of liquid clouds that rain from November 2006 to October 2010 obtained from the RAIN-PROFILE data files. The red lines indicate plus or minus one standard deviation obtained across 100 subsets of 400 randomly selected cold fronts. The vertical dotted line indicates the location of the surface front.

otherwise, the water content is rather uniform across the region and decreases with increasing altitude. Figure 7b demonstrates that the variability of the cloud liquid water content profiles is large along the lower boundary where the surface starts to impact the retrievals (Lebsack et al. 2011).

4. Environmental impact on clouds and precipitation across cold fronts

Clouds and precipitation in extratropical cyclones are the result of moisture convergence and vertical motions (e.g., Stewart et al. 1998). Indeed, both mean column-integrated precipitable water within the cyclone and the

strength of the cyclone (as characterized by wind speed for example) have a large impact on the amount of clouds in the warm frontal zone (Field and Wood 2007; Naud et al. 2012). Here we explore the impact of the strength of the ascent and the mean precipitable water on the cold frontal clouds and precipitation. Temperature within the cyclones will also influence clouds and precipitation, and so we also investigate the impact of the mean surface potential temperature within the cyclone (to account for the latitudinal change in sea level pressure and cyclone strength). In addition, as a coarse approximation for the temperature gradient at the cold front, we examine the impact of the contrast in temperature between the warm and cold sector across the surface cold front.

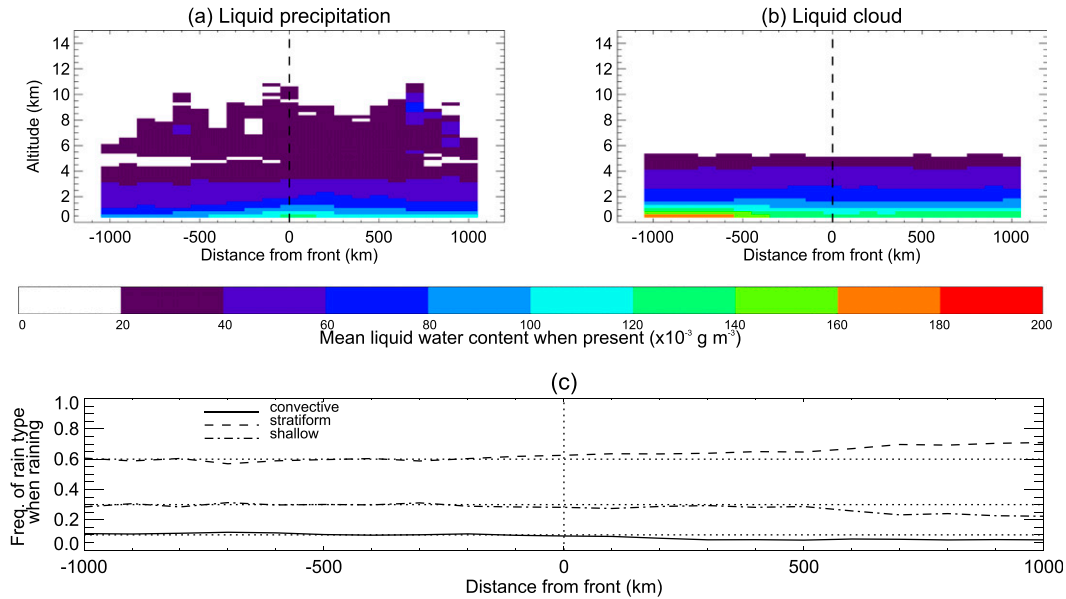


FIG. 6. Mean liquid water content profiles across cold fronts in the midlatitudes (30° – 60° N and 30° – 60° S) from November 2006 to October 2010 for (a) precipitation and (b) clouds, obtained from the RAIN-PROFILE retrievals. (c) Across cold front composite of surface precipitation type frequency, with convective (solid), stratiform (dashed), and shallow (dot-dashed) extracted from the PRECIP-COLUMN data files. The vertical dashed line indicates the location of the surface front.

For each cyclone in our database, we extract MERRA column-integrated precipitable water (PW), 500-hPa vertical velocity (ω), and surface potential temperature (θ_s) in a region of 25° radius centered on the low pressure center. These three quantities are reprojected from the regular latitude–longitude grid into a stereographic grid centered on the low. These grids are then rotated so that all of the cold fronts are aligned along a north–south direction with the center of rotation defined as the intersect between the latitude of the low and the linearly regressed general direction of the cold front. For each cold front, PW and θ_s are then averaged in the region centered on the cold front ± 1000 km across and 1000 km along the cold front equatorward from the latitude of the low. Because we want to characterize the strength of the

cyclones using only the strength of the ascent, ω values are averaged only in the region to the east of the cold fronts where it is negative (i.e., ascending). Having characterized each of the cold fronts with these parameters, we add a fourth parameter, the surface potential temperature contrast ($\Delta\theta_s$), by calculating the difference in average θ_s in the half region to the east of the front minus the half region to the west of the front.

For our entire database (four years, two hemispheres), we first evaluate how these four metrics are correlated (see Table 1). Not surprisingly, the amount of moisture across the cold front is highly correlated with the surface potential temperature (i.e., the warmer the environment, the more moisture it contains). However, the correlation coefficients between the other pairs are

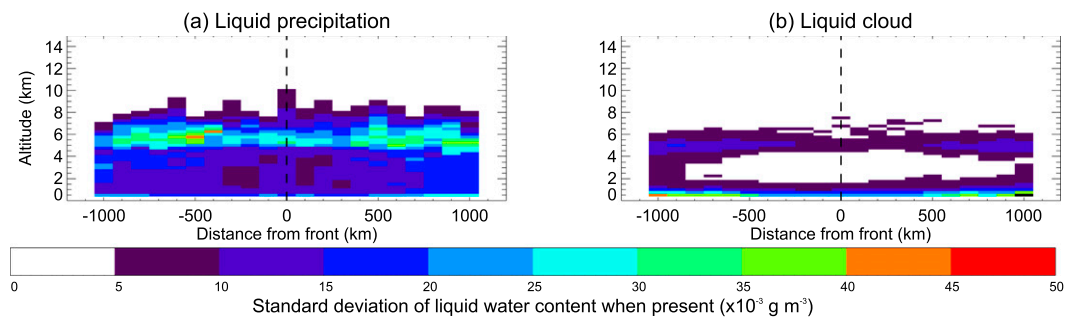


FIG. 7. Standard deviation across 100 subsets of 400 randomly selected cold fronts of liquid water content in (a) precipitation and (b) cloud. The vertical dashed line indicates the location of the surface front.

TABLE 1. Correlation coefficient between the four cold front metrics (PW, ω , θ_s , and $\Delta\theta_s$) for the entire 4-year NH and SH cold front database.

Metrics	PW	ω	θ_s	$\Delta\theta_s$
PW	1.00	0.06	0.85	0.23
ω	0.06	1.00	-0.05	-0.18
θ_s	0.85	-0.05	1.00	0.36
$\Delta\theta_s$	0.23	-0.18	0.36	1.00

low. The amount of moisture in the environment and the contrast in temperature across the cold front are positively correlated (i.e., cyclones with more available moisture tend to have a greater contrast in temperature across the cold front); however, the correlation coefficient is only 0.23. This suggests that indeed the difference in potential temperature between the two sides of the cold front is not a perfect approximation of the actual temperature gradient across the cold front.

To examine the influence of each metric, we decided to contrast the impact of the larger values versus that of the lower values, similar to the conditional subsetting method proposed in Booth et al. (2013). For this, we subset our cold front database into two populations for each metric: cold fronts in the upper 10th percentile and cold fronts in the lower-10th percentile. Note that the strength of the ascent is given by negative values, and hence the ascent-based subsets are defined based on the absolute value of the mean vertical velocity. For each subset, we again composite the cloud frequency of occurrence, the cloud-type frequency of occurrence, and the precipitation characteristics across the cold fronts

and plot the difference between the two opposite subsets to examine the impact of each environmental factor on the cold fronts.

Looking first at the impact on cloud cover (Fig. 8), PW tends to favor the occurrence of high-level clouds but surprisingly is associated with decreased cloud occurrence below about 8 km, and in particular in the first 2 km above the surface on the western side of the front (Fig. 8a). The possible reasons for this are further discussed below. Through their high correlation, PW and surface potential temperature impacts are very similar (Fig. 8a vs Fig. 8b), although we note some slight differences: the impact of PW on high clouds is significantly larger than the impact of temperature (about 10%), while temperature has a larger negative impact than moisture on the cloud occurrence between the surface and 6 km in the region of the cold front. We find that the cold fronts that populate the upper (lower) 10% PW subset are distinct from those that populate the upper (lower) 10% θ_s subset.

More quantitatively, we find that the mean PW for the upper 10% is ~ 39 mm while it is 9 mm for the lowest 10%, which implies that a quadrupling of PW causes more than a 30% increase in high-level cloud frequency of occurrence on the eastern side and a $\sim 25\%$ decrease in low-level cloud frequency of occurrence on the western side of the cold front. Using the radar-only cloud detections, we verified that the decrease in low-level clouds was not caused by the impact on the lidar signal of an increase in high-level clouds. The difference in potential temperature between the upper and lower 10% is about 20 K, which

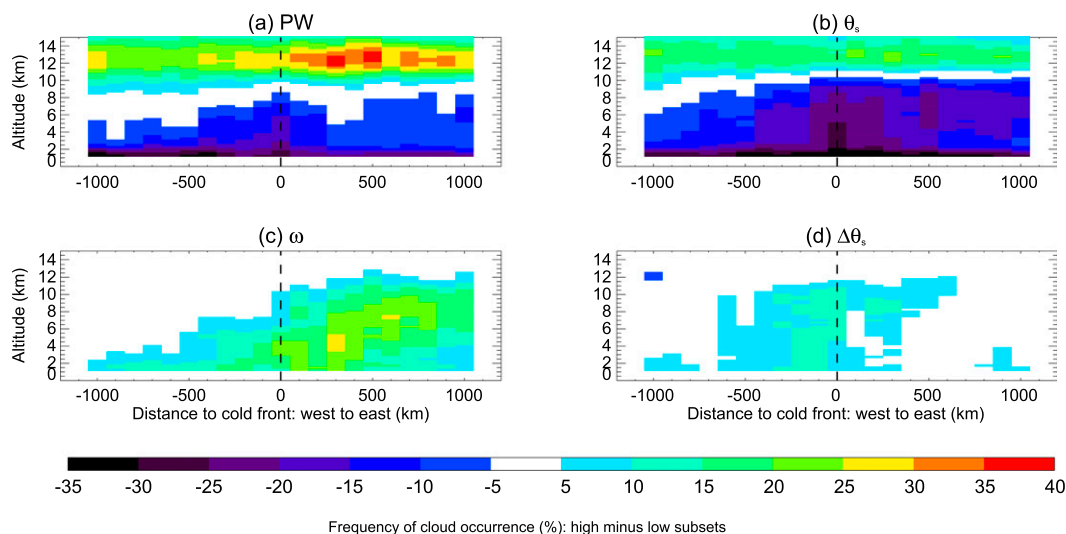


FIG. 8. Difference in cloud frequency of occurrence across cold fronts between the 10% highest and 10% lowest (a) PW, (b) θ_s , (c) ω , and (d) $\Delta\theta_s$ averaged for each cold front within ± 1000 km east/west and within 1000 km of the low pressure center along the front. The vertical dashed line indicates the location of the surface front. The differences are greater than one standard deviation (Fig. 2).

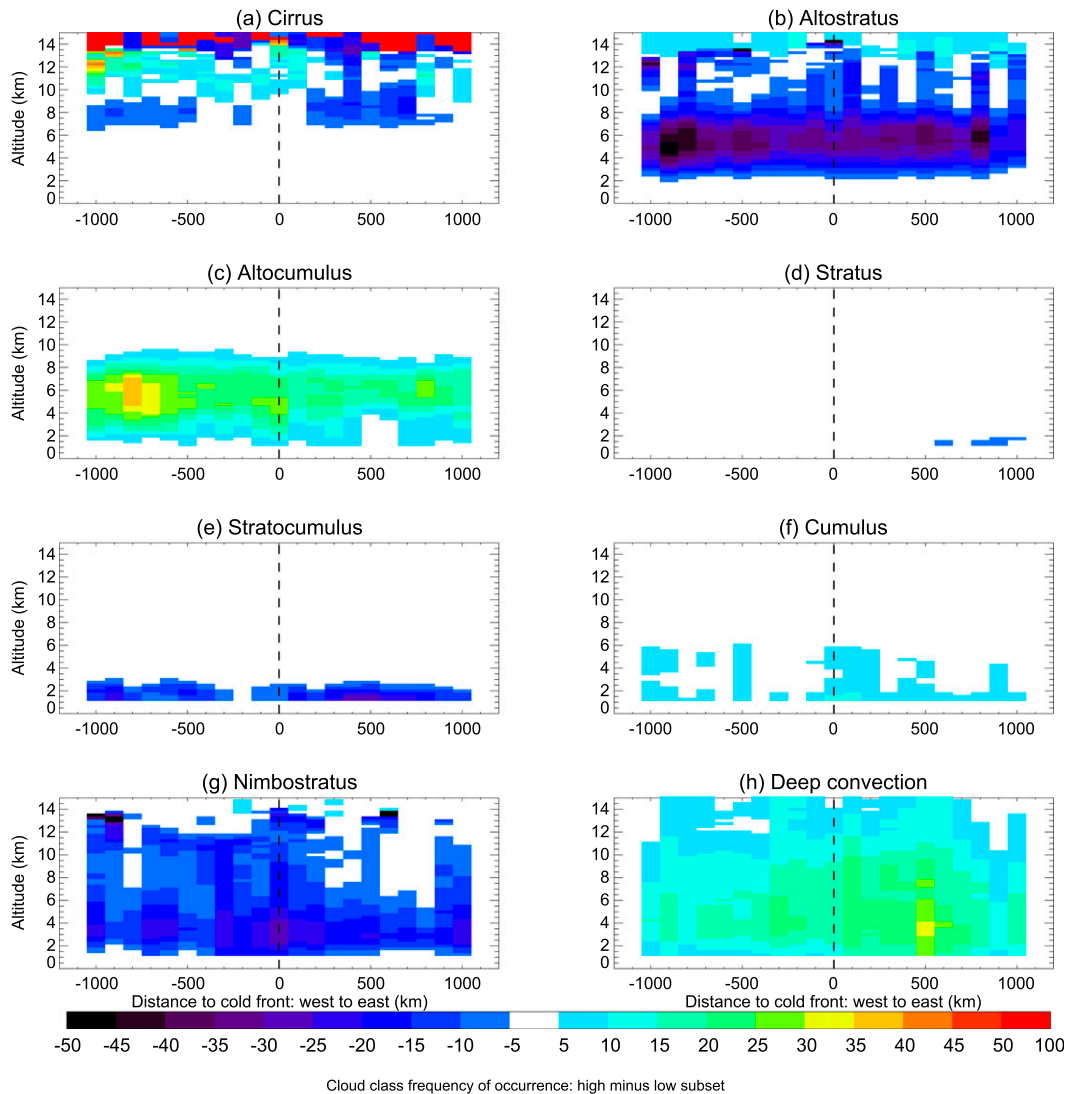


FIG. 9. Difference in the frequency of occurrence of each cloud type between cold fronts with 10% top and 10% bottom PW subsets. The vertical dashed line indicates the location of the surface front. The differences are greater than one standard deviation (Fig. 4).

causes a decrease of about 30% in low-level cloud frequency of occurrence across the region and an increase of up to 25% in high-level clouds on the eastern side.

As the ascent strength increases (i.e., a decrease in vertical velocity in pressure coordinates; Fig. 8c), cloud frequency of occurrence increases by 5%–10% at low levels on the western side and at all levels on the eastern side of the front, with a maximum impact (above 20% increase) that slowly rises from west to east. In the upper 10% subset in ω , the mean ascent is -10.9 hPa h^{-1} , while it is on average -1.6 hPa h^{-1} in the lower 10% subset. Therefore, for a sevenfold increase in ascent strength, cloud frequency of occurrence increases by more than 20% on the eastern side and 5%–10% on the western side of the front.

As the across cold front contrast in temperature increases (Fig. 8d), the frequency of cloud occurrence within 500 km west of the front increases from the surface to $\sim 10 \text{ km}$ and from ~ 4 to 10 km within 500 km east of the front. The difference in temperature contrast between the upper and lower 10% subsets is about 14 K and causes an increase in cloud frequency of 5%–10% and up to 15%, 100 km west of and at the cold front, respectively.

The relatively large decrease in low- and midlevel clouds that accompanies an increase in moisture and temperature is surprising. Therefore, we now investigate the impact of an increase in moisture on the distribution of cloud types. Figure 9 shows the difference in frequency of occurrence of each cloud type (this time

including clear profiles) between the cold fronts with the largest PW and those with the lowest. It indicates that more moisture favors the occurrence of deep convective, cumulus, and altocumulus clouds but reduces the occurrence of altostratus, nimbostratus, and stratocumulus clouds. Cirrus clouds tend to be displaced upward, and there is also some indication that the same happens to altostratus clouds (not shown). This is probably caused by the difference in tropopause altitude between warm and cold cases. Overall, it appears that enhancements in moisture result in a replacement of the stratiform clouds with convective clouds. The impact of an increase in surface potential temperature is similar (not shown), although the reduction in nimbostratus and increase in cumulus are slightly larger. The impacts of ascent strength and temperature contrast on cloud type at the cold front are of relatively small importance and hence are also not shown. The ascent strength favors the occurrence of nimbostratus clouds across the entire region to the detriment of altocumulus and cirrus clouds. The temperature contrast across the cold fronts also favors the occurrence of nimbostratus clouds, although to a lesser degree than the ascent strength and mostly to the west of the cold front, while it also favors the occurrence of altostratus clouds to the west. High clouds also happen more often across the front when the temperature contrast is large, possibly related to enhanced baroclinicity that would enhance the detrainment of mass.

These changes in cloud type as the environment changes are consistent with the changes in precipitation characteristics. The negative impact of potential temperature is larger than the impact of moisture on rain rates (Fig. 10a), which comes from a larger diminution in frequency of occurrence of rain (Fig. 10c), consistent with a greater reduction in the frequency of occurrence of nimbostratus clouds. Overall, additional moisture or greater environmental temperature acts to suppress precipitation, specifically to the west of and at the surface front. Presumably, the enhancement of convection causes the impact to be somewhat neutral to the east (i.e., convective rain replaces stratiform rain). This is confirmed by the diminution in the fraction of liquid clouds that rain, suggesting that the deeper, mixed-phase convective clouds are dominating the rain formation. That said, we cannot exclude that because the *CloudSat* radar signal becomes saturated in situations of heavy convective rain, changes in rain rates may not be measurable, causing a near-zero difference.

The ascent strength enhances precipitation across the entire region with a peak in the first 500 km to the east of the cold front (Fig. 10a). Although the impact of ascent strength on the rain rates when it is raining is relatively uniform across the region (Fig. 10b), the peak is caused

by an increase in the frequency of occurrence of rain (Fig. 10c), while the increase in snow frequency is rather uniform across the region (Fig. 10d). The fraction of liquid clouds that rain increases with ascent strength to the west of the front (Fig. 10e). The impact of the temperature contrast is small compared to the impact of the other factors, and the difference between the two extreme subsets is mostly within the variability shown in Fig. 5. There is a slightly greater rain rate when raining at the cold front when the contrast is largest (Fig. 10b).

The impact of the ascent and across cold front contrast in temperature on water content profiles in precipitation and liquid clouds is barely noticeable, so we have chosen not to show it. The ascent strength only slightly increases water content in liquid precipitation at low levels to the east and liquid water in clouds across the entire region in the very first kilometer above the surface. No clear signal can be observed regarding the effect of the cold front temperature contrast. Because the environmental temperature and moisture impacts are virtually identical, we only show the latter. Figure 11a demonstrates that the larger the moisture (or temperature), the larger the water content in liquid precipitation. As moisture increases, liquid water content in clouds tends to diminish below 2 km and increases between 4 and 6 km (Fig. 11b). An examination of mean water content separately for the high and low PW subsets reveals that 1) the cloud liquid water content is more uniform for the high PW subset while low PW gives much greater water contents below 3 km, and 2) the clouds themselves extend to higher altitudes for larger PW values, although it is hard to tell without a distribution whether some are moved upward or if they are on average deeper.

Our experiments reveal that because moisture and temperature are highly correlated, they are relatively equivalent in describing the thermodynamic conditions within the cyclones. An increase in moisture and/or temperature tends to favor the occurrence of convective clouds and precipitation, but this happens at the detriment of stratiform clouds and precipitation. Consequently, cold fronts in warm and wet conditions exhibit, on average, less cloud cover and less total precipitation than in colder and drier environments. In contrast, the strength of the ascent has a positive impact on both cloud and precipitation to the west of the front as well as to the east. The contrast in temperature between the eastern and western sides of the cold fronts has a more modest impact on both clouds and precipitation than the other parameters we tested here but, nevertheless, a larger contrast tends to favor cloud formation to the west of the front and impacts rain rates. Now that we know what impact these environmental parameters have on clouds and precipitation across the cold front,

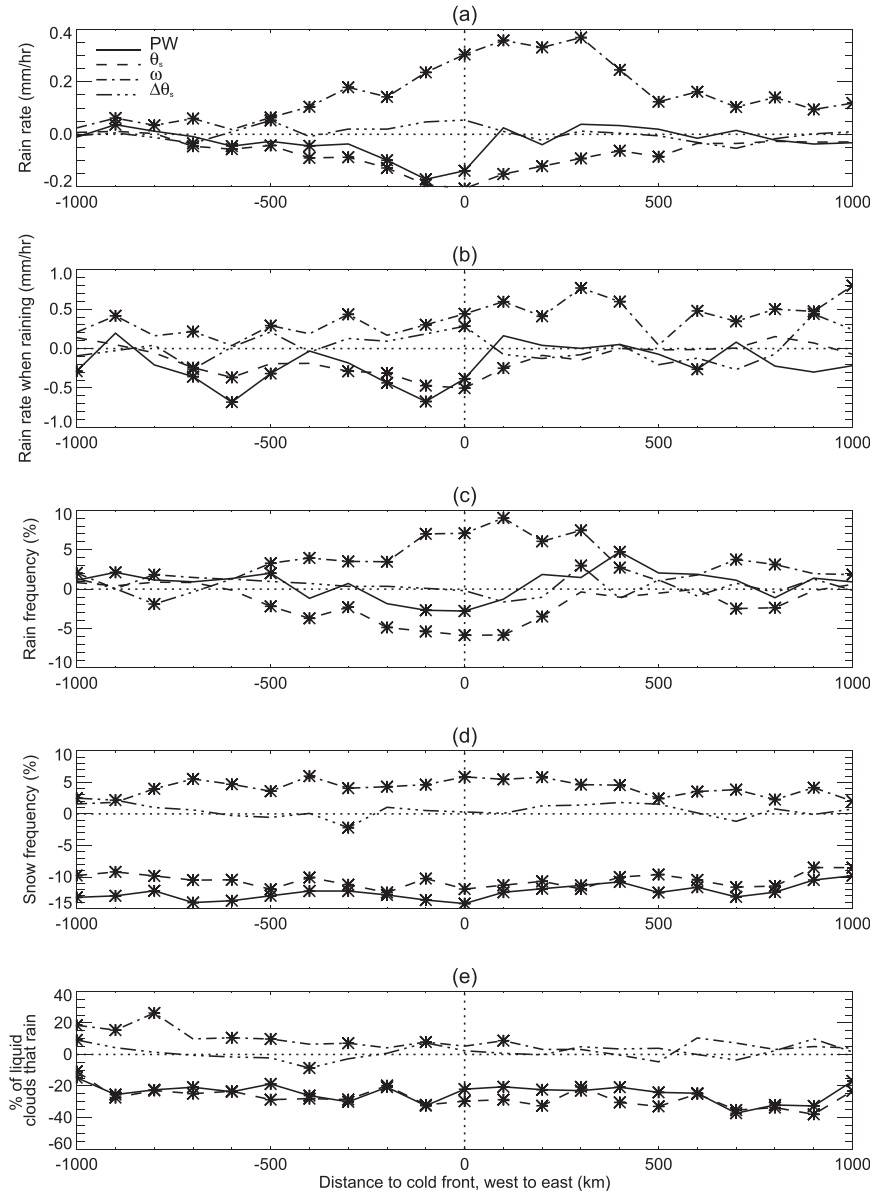


FIG. 10. Difference between the subsets with highest value and lowest value of PW (solid), θ_s (dashed), ω (dot-dashed), and $\Delta\theta_s$ (three dots-long dash) in (a) rain rate, (b) rain rate when raining, (c) rain frequency of occurrence, (d) snow frequency of occurrence, and (e) percentage of liquid clouds that rain. The vertical dashed line indicates the location of the surface front. The asterisks along each line indicate the 100-km bins where the difference is above one standard deviation as given in Fig. 5.

we examine if they can help to explain seasonal and hemispheric differences.

5. Seasonal and hemispheric contrast in cloud and precipitation across cold fronts

The manner in which seasonal and hemispheric differences in temperature, moisture amount, and cyclone

characteristics influence the seasonal and hemispheric contrast in cold frontal cloud and precipitation is now examined.

First we explore seasonal and hemispheric differences in cold front mean PW, θ_s , ω , and $\Delta\theta_s$. Figure 12 shows the distribution of these four parameters for each subset defined as all NH and all SH cold fronts as well as each season per hemisphere. Focusing first on the

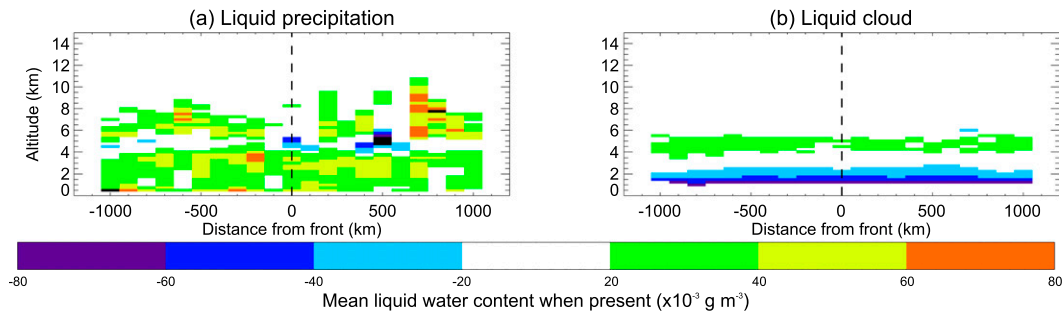


FIG. 11. Difference in mean liquid water content when present between upper and lower 10th percentile subsets on PW for (a) precipitation and (b) cloud. The vertical dashed line indicates the location of the surface front. Differences less than one standard deviation as given in Fig. 7 are not shown.

hemispheric differences, the figure indicates that, on average, NH cold fronts are moister and warmer, with a weaker ascent but larger across-front temperature contrast. This finding is consistent with Naud et al. (2012) for warm fronts. However, here we do not attempt to constrain the meridional distribution of the cold fronts, which entails that there are proportionally more cold fronts in the highest latitudinal range (50° – 60°) in the SH than NH. This can partly explain the colder and drier conditions in the SH cold fronts than in those in the NH. Based on the impact of these different cold front parameters on cloud frequency of occurrence, one would expect a much larger high-level cloud cover and lower low- and midlevel cloud cover in the NH than in the SH.

Figure 13 shows the difference in cloud frequency of occurrence between the NH and the SH where it is larger than the one standard deviation shown in Fig. 2. It indeed demonstrates a much larger (5%–10%) frequency of occurrence of high-level clouds in the NH than in the SH. There are, however, slightly more low-level clouds in the SH than in the NH in the eastern sector and on the extreme western edge of the region, away from the surface front. If moisture, temperature, and ascent strength were the only factors affecting the cloud occurrence, one would expect much larger differences in low- and midlevel clouds (cf. Fig. 8). However, Fig. 12d suggests that at low and midlevels, the impact of additional moisture or temperature in the NH may be partly compensated by the impact of a greater across-front temperature contrast.

To explore the seasonal variations in cloud frequency of occurrence, we then examined the difference between the composite for each season and the yearly composite of cloud frequency of occurrence, separately for each hemisphere. Figure 14 indicates that the seasonal variations in cloud frequencies are similar in the two hemispheres for winter and summer but that the variations are much smaller in the SH than in the NH. In fact, the winter–summer differences in frequency of cloud

occurrence barely exceed 5% in the SH. In contrast, the NH differences for these two seasons exceed 10%. For both hemispheres, winter cold fronts have more low- and midlevel clouds than the yearly average but fewer high-level clouds; summer cold fronts show the opposite (i.e., more high-level and fewer mid- and low-level clouds than the yearly average). In view of the large impacts of moisture and/or temperature (Figs. 8a and 8b), the larger winter–summer contrast in the NH compared to the SH (Figs. 12a and 11c), and the additional impact of stronger winter ascent (Figs. 8c and 12b), the winter–summer contrast in cloud frequency of occurrence can be explained by the seasonal contrast in temperature and moisture.

From Fig. 12 we observe that in spring, cold front properties are close to winter properties, while the fall characteristics are more similar to those of the summer. This is also evident for both hemispheres' cloud frequency of occurrence (Fig. 14), with the SH intermediate seasons being less contrasted than their NH counterparts.

The rain rates are fairly similar between seasons in the SH, consistent with the seasonal variations in cloud cover, with slightly greater rain rates in winter just east of the surface front (Fig. 15a). The seasonal contrast in the NH is much larger (consistent with Ellis et al. 2009), with winter rain rates above and summer rain rates below the yearly average from 500 km west all the way to 1000 km east of the surface front. Interestingly, the intermediate seasons are not a weaker replicate of winter and summer: in spring the rain rates west (east) of the surface front follow the winter (summer) anomalies, and vice versa for the fall anomalies. Rain rates when raining (Fig. 15b) vary little from one season/hemisphere to another, with the envelope limited by the NH winter rates for the larger rates and NH summer for the lower rates. Again, the SH values display very small seasonal variations compared to the NH.

Rain frequency of occurrence (Fig. 15c) also displays little seasonal variation in the SH, but spring NH rain

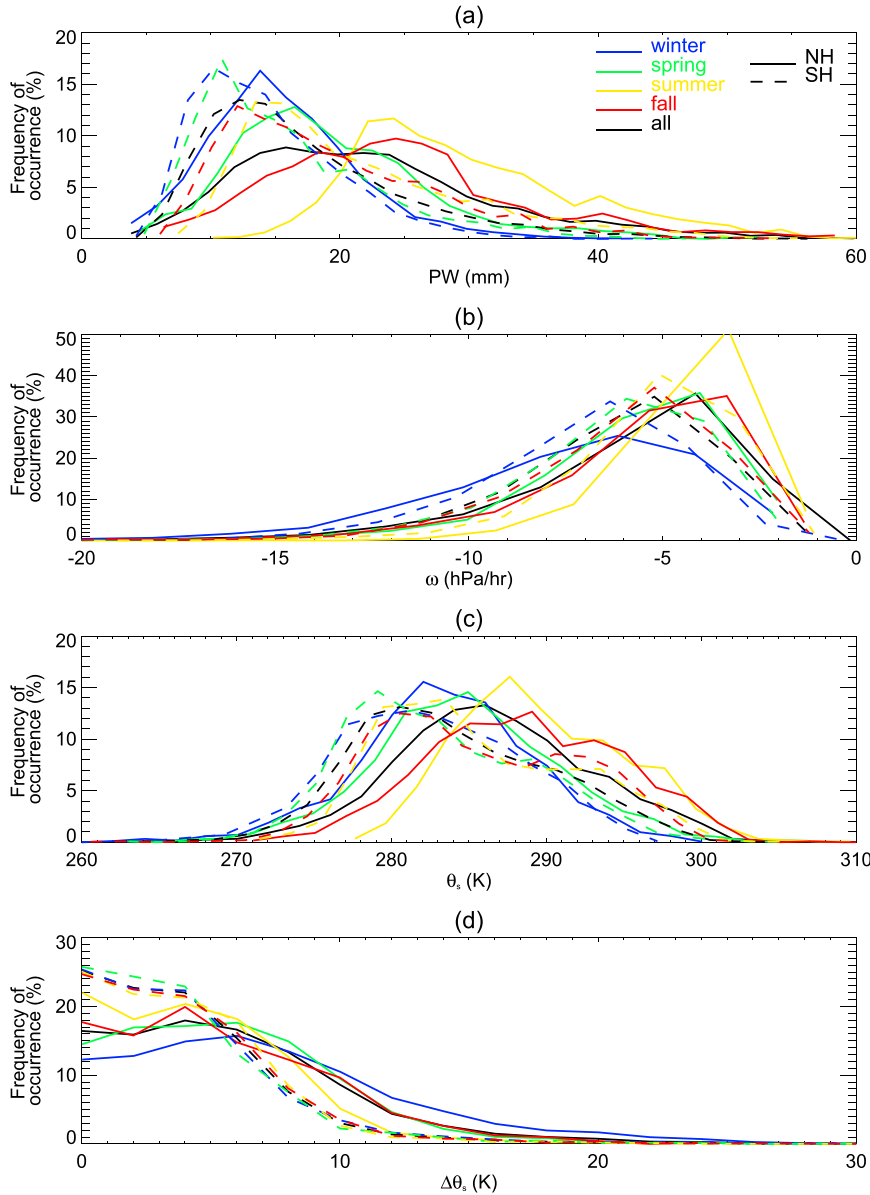


FIG. 12. Frequency of occurrence of cold front properties in the NH (solid) and the SH (dashed) for all seasons (black), winter (blue), spring (green), summer (yellow), and fall (red): (a) PW, (b) ω , (c) θ_s , and (d) $\Delta\theta_s$.

frequency is the largest to the west of the front (and above the one standard deviation shown in Fig. 5). This is surprising given the lack of anomalous cloud frequency of occurrence (Fig. 14). We also note that in the SH, the anomaly in the springtime rain frequency west of the surface front is larger than for the other seasons (although not significantly). In contrast, snow frequency (Fig. 15d) in the NH spring is lower than the winter and fall values. For the NH, snow frequency is largest in winter and close to null in summer, with fall values larger than spring values. In the SH, snow occurs

throughout the year, with a maximum in winter and minimum in summer, and spring and fall values are very close. Finally, the percentage of liquid clouds that precipitate (Fig. 15e) displays a fairly large variability, but there is no clear difference between seasons and hemispheres, although summertime values to the west of the front tend to be the lowest in both hemispheres, and in the NH these values stay low to the east of the front.

Overall, the precipitation statistics are consistent with the cloud-cover statistics, with the SH showing very little variability compared to the NH seasonal variations, and

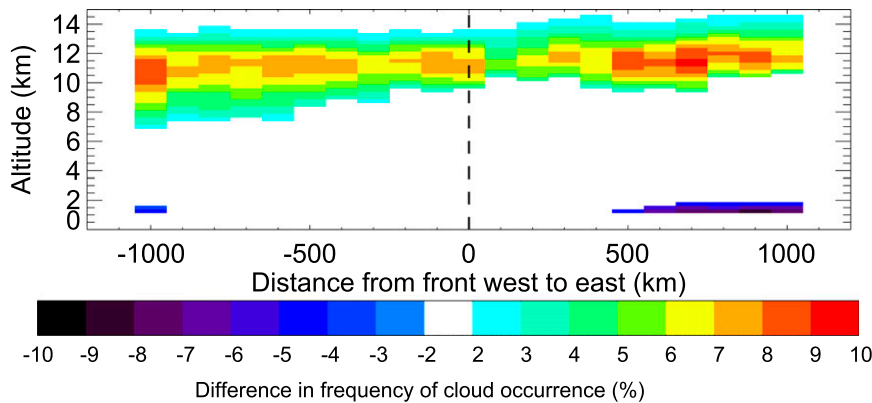


FIG. 13. Difference in frequency of cloud occurrence between NH and SH cold fronts for all seasons. The vertical dashed line indicates the location of the surface front. The difference is only shown when larger than one standard deviation as represented in Fig. 2.

with a large NH contrast between winter and summer. One surprising result is the relatively large frequency of occurrence of rain in the postfrontal zone and fairly large rain rates at the surface front during spring in the NH. An assessment of the profiles of water content in liquid precipitation and liquid cloud (not shown) did not reveal any seasonal differences that were inconsistent with the surface precipitation characteristics and cloud cover. In particular, the water content in liquid precipitation in NH spring is not significantly different than in the other seasons, confirming that it is the frequency of occurrence of rain that is larger in spring and not the amount of rain itself. When we compare the cloud type frequency of occurrence between spring and winter, focusing on the cloud types present in the western sector, we find slightly more nimbostratus and stratocumulus clouds but significantly more altocumulus in spring than in winter. However, it is unclear what factors may influence this difference between spring and winter rain frequency, as seasonal variations in Fig. 12 are small and anomalies in Fig. 10 are also small in the western sector. This suggests that the environmental factors studied here, even if dominant, may not be enough to explain the seasonal changes in cold front precipitation.

6. Conclusions

The cloud and precipitation characteristics across midlatitude cold fronts have been examined using 4 years of *CloudSat* and *CALIPSO* retrievals of cloud vertical distribution, cloud type, and precipitation characteristics. The datasets show that cloud cover is at a maximum at low altitudes (below 3 km) across the entire region from 1000 km west to 1000 km east of the surface front. Another area of relatively large cloud cover is found east of and within 500 km of the surface front, with

clouds extending upward from the surface to about 14 km. Stratocumulus clouds dominate the western side of the cold fronts, while nimbostratus, altostratus, and cirrus clouds dominate the eastern side of the front. The peak in rain rates is slightly east of the surface front as is the peak in rain frequency of occurrence. The rain rates when raining are larger to the east than to the west of the surface front. Snow is more frequent to the west of the cold front. The fraction of liquid clouds that rain is larger to the east than to the west of the surface front. The precipitation liquid water content peaks at low levels slightly east of the cold front, while the cloud liquid water content is at a maximum to the west.

Environmental moisture and temperature have a similar relationship with the cloud and precipitation characteristics across the cold front because of the high correlations between moisture and temperature. Increases in moisture and surface potential temperature are found alongside increased occurrence of clouds above 10 km but reduced occurrence of clouds below 10 km. Similarly, enhancements in moisture and temperature tend to be associated with reduced precipitation, mostly to the west of the front, in rain rate and frequency of occurrence, while there is a reduction in snow frequency and the fraction of clouds that precipitate across the entire region. Liquid water contents in precipitation and clouds expand upward when temperature and moisture contents are greater, as liquid persists to higher altitudes, but the maximum in liquid water content decreases in cloud and increases in precipitation. Their impact alone can explain the contrast between summer and winter cloud and precipitation characteristics—a contrast that is much larger in the Northern than Southern Hemisphere where more cold fronts can be found at higher latitudes. The strength of the ascent and the strength of the temperature contrast

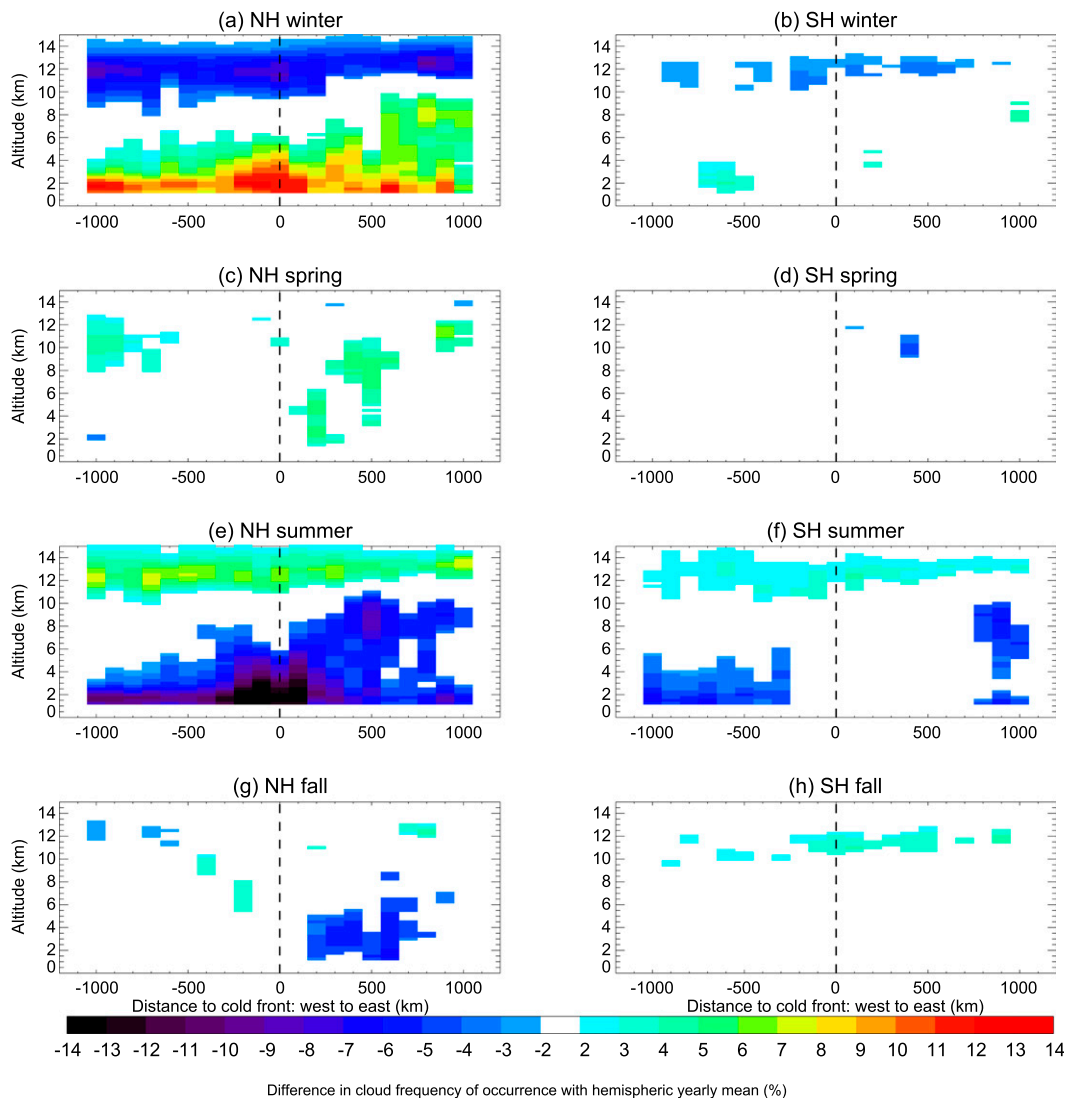


FIG. 14. Difference in cloud frequency of occurrence between the mean per season and the yearly mean per hemisphere for (a),(c),(e),(g) NH and (b),(d),(f),(h) SH: (a),(b) winter; (c),(d) spring; (e),(f) summer; and (g),(h) fall. The vertical dashed lines indicate the location of the surface front. Differences below one standard deviation as given in Fig. 2 are not shown.

across the cold fronts both work to enhance low- and midlevel clouds in the entire region for the former and in the postfrontal region for the latter. The impact of the strength of the ascent on precipitation rates and frequency of occurrence is large, but the temperature contrast has little influence. While the strength of the ascent contributes to the contrast in the cloud and precipitation between winter and summer in both hemispheres, the temperature contrast across the front may help to partly explain the hemispheric difference: warmer and wetter conditions in the NH support the greater occurrence of high-level clouds there, but the small difference between the two hemispheres at

middle and low levels may be caused by the impact of the greater across-front contrast in temperature in the NH that compensates the impact of moisture/temperature.

Although the moisture, temperature, ascent, and east–west temperature contrast play a significant role for the cloud and precipitation across the cold frontal region, they were insufficient to explain some of the more subtle differences. One example is the large frequency of occurrence of rain to the west of the front in the spring compared to all other three seasons. Another factor that we have not considered here is the presence of aerosols (Igel et al. 2013). MODIS aerosol optical thickness retrievals averaged in the cold front region are greater in

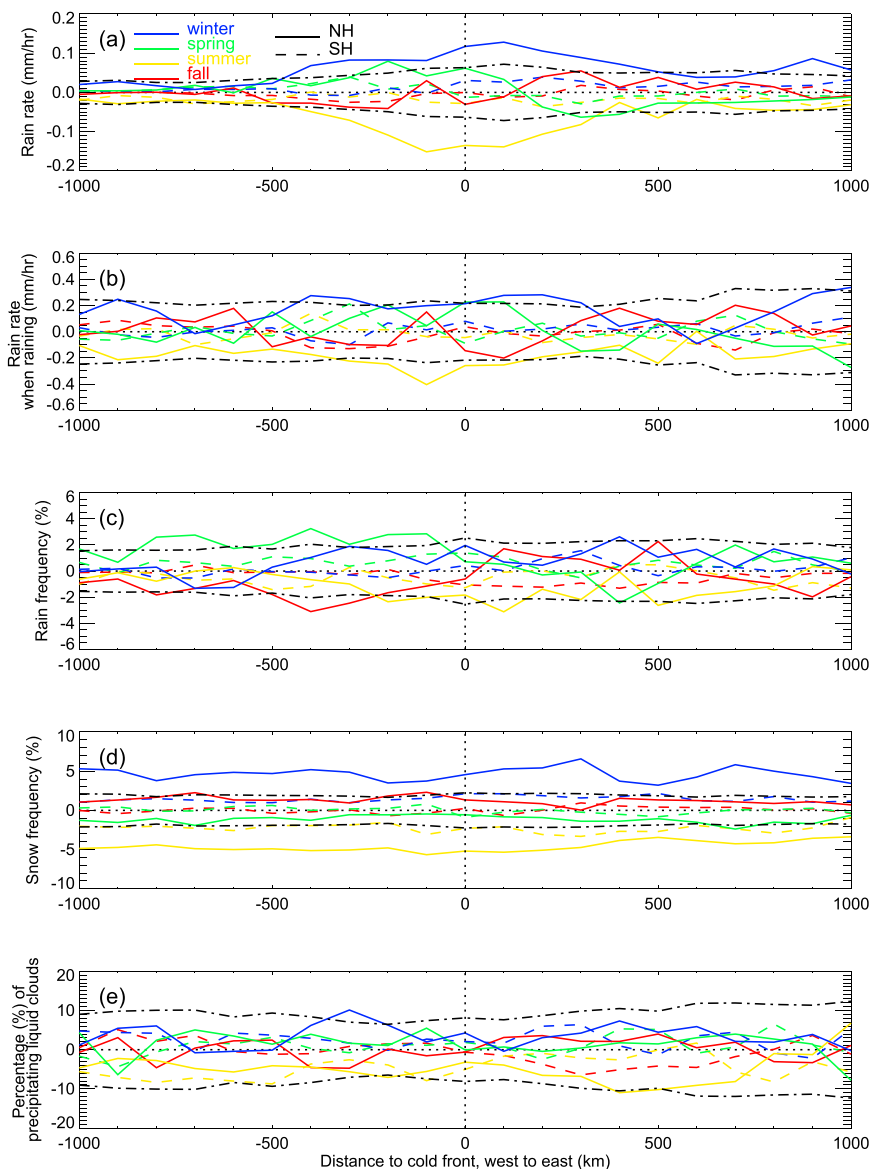


FIG. 15. Anomaly of NH and SH seasonal composites across cold fronts against yearly mean of (a) rain rate, (b) rain rate when raining, (c) rain frequency of occurrence, (d) snow frequency of occurrence, and (e) percentage of liquid clouds that rain. The vertical dashed line indicates the location of the surface front. The dot-dashed lines represent the plus or minus one standard deviation represented in red in Fig. 5.

the Northern Hemisphere than in the Southern Hemisphere and peak in the spring. However, before we can investigate the impact of aerosols further, additional detailed analysis of sampling issues in the context of fairly cloudy environments is necessary. The exact role of aerosols will therefore be the subject of a future, more detailed, and separate investigation.

The finding that precipitation and cloudiness are lower in the wetter environments does not exclude the possibility that the more extreme rain rates happen

more often. The transition between more stratiform rain in a colder environment to more convective rain in a warmer environment may attest to that. Composites are powerful tools to get at the most salient features of a phenomenon but, as such, do not explain the underlying variability. We also note that the impact of moisture on the warm front is opposite to what we have seen here for cold fronts: more moisture favors cloud occurrence and precipitation along the warm fronts (e.g., Field and Wood 2007).

Acknowledgments. The *CloudSat*–*CALIPSO* products were obtained from the *CloudSat* Data Processing Center. The MERRA outputs were obtained from the Goddard Earth Sciences Data and Information Services Center. The MCMS dataset, documentation, and algorithm are available at <http://gcss-dime.giss.nasa.gov/mcms/>. We thank Mike Bauer for the ERA-Interim-based dataset. This work is funded by the NASA *CloudSat* Science Team Reconnect Grant NNX13AQ33G. CMN is also funded by NASA the Science of *Terra* and *Aqua* Grant NNX11AH22G. We thank the editor and three anonymous reviewers for helping us significantly improve this manuscript.

REFERENCES

- Bauer, M., and A. D. Del Genio, 2006: Composite analysis of winter cyclones in a GCM: Influence on climatological humidity. *J. Climate*, **19**, 1652–1672, doi:10.1175/JCLI3690.1.
- Berry, G., C. Jakob, and M. Reeder, 2011: Recent global trends in atmospheric fronts. *Geophys. Res. Lett.*, **38**, L21812, doi:10.1029/2011GL049481.
- Bjerknes, J., and H. Solberg, 1922: Life cycle of cyclones and the polar front theory of atmospheric circulation. *Geophys. Publ.*, **3** (1), 1–18.
- Booth, J. F., C. M. Naud, and A. D. Del Genio, 2013: Diagnosing warm frontal cloud formation in a GCM: A novel approach using conditional subsetting. *J. Climate*, **26**, 5827–5845, doi:10.1175/JCLI-D-12-00637.1.
- Browning, K. A., 1986: Conceptual models of precipitation systems. *Wea. Forecasting*, **1**, 23–41, doi:10.1175/1520-0434(1986)001<0023:CMOPS>2.0.CO;2.
- Catto, J. L., and S. Pfahl, 2013: The importance of fronts for extreme precipitation. *J. Geophys. Res.*, **118**, 10 791–10 801, doi:10.1002/jgrd.50852.
- , C. Jakob, G. Berry, and N. Nicholls, 2012: Relating global precipitation to atmospheric fronts. *Geophys. Res. Lett.*, **39**, L10805, doi:10.1029/2012GL051736.
- , N. Nicholls, C. Jakob, and K. L. Shelton, 2014: Atmospheric fronts in current and future climates. *Geophys. Res. Lett.*, **41**, 7642–7650, doi:10.1002/2014GL061943.
- Dee, D. P., and Coauthors, 2011: The ERA-Interim reanalysis: Configuration and performance of the data assimilation system. *Quart. J. Roy. Meteor. Soc.*, **137**, 553–597, doi:10.1002/qj.828.
- Ellis, T. D., T. L'Ecuyer, J. M. Haynes, and G. L. Stephens, 2009: How often does it rain over the global oceans? The perspective from *CloudSat*. *Geophys. Res. Lett.*, **36**, L03815, doi:10.1029/2008GL036728.
- Feser, F., M. Barcikowska, O. Krueger, F. Schenk, R. Weisse, and L. Xia, 2015: Storminess over the North Atlantic and northwestern Europe—A review. *Quart. J. Roy. Meteor. Soc.*, **141**, 350–382, doi:10.1002/qj.2364.
- Field, P. R., and R. Wood, 2007: Precipitation and cloud structure in midlatitude cyclones. *J. Climate*, **20**, 233–254, doi:10.1175/JCLI3998.1.
- Govekar, P. D., C. Jakob, M. J. Reeder, and J. Haynes, 2011: The three-dimensional distribution of clouds around Southern Hemisphere extratropical cyclones. *Geophys. Res. Lett.*, **38**, L21805, doi:10.1029/2011GL049091.
- Haynes, J. M., T. S. L'Ecuyer, G. L. Stephens, S. D. Miller, C. Mitrescu, N. B. Wood, and S. Tanelli, 2009: Rainfall retrieval over the ocean with spaceborne W-band radar. *J. Geophys. Res.*, **114**, D00A22, doi:10.1029/2008JD009973.
- Hewson, T. D., 1998: Objective fronts. *Meteor. Appl.*, **5**, 37–65, doi:10.1017/S1350482798000553.
- , and H. A. Tittley, 2010: Objective identification, typing and tracking of the complete life-cycles of cyclonic features at high spatial resolution. *Meteor. Appl.*, **17**, 355–381, doi:10.1002/met.204.
- Hobbs, P. V., 1978: Organization and structure of clouds and precipitation on the mesoscale and microscale in cyclonic storms. *Rev. Geophys.*, **16**, 741–755, doi:10.1029/RG016i004p00741.
- Igel, A. L., S. C. van den Heever, C. M. Naud, S. M. Saleeby, and D. J. Posselt, 2013: Sensitivity of warm-frontal processes to cloud-nucleating aerosol concentrations. *J. Atmos. Sci.*, **70**, 1768–1783, doi:10.1175/JAS-D-12-0170.1.
- Kunkel, K. E., D. R. Easterling, D. A. R. Kristovich, B. Gleason, L. Stoecker, and R. Smith, 2012: Meteorological causes of the secular variations in observed extreme precipitation events for the conterminous United States. *J. Hydrometeorol.*, **13**, 1131–1141, doi:10.1175/JHM-D-11-0108.1.
- , and Coauthors, 2013: Monitoring and understanding trends in extreme storms. *Bull. Amer. Meteor. Soc.*, **94**, 499–514, doi:10.1175/BAMS-D-11-00262.1.
- Lau, N.-C., and M. W. Crane, 1995: A satellite view of the synoptic-scale organization of cloud properties in midlatitude and tropical circulation systems. *Mon. Wea. Rev.*, **123**, 1984–2006, doi:10.1175/1520-0493(1995)123<1984:ASVOTS>2.0.CO;2.
- , and —, 1997: Comparing satellite and surface observations of cloud patterns in synoptic-scale circulation systems. *Mon. Wea. Rev.*, **125**, 3172–3189, doi:10.1175/1520-0493(1997)125<3172:CSASOO>2.0.CO;2.
- Lebsock, M. D., and T. S. L'Ecuyer, 2011: The retrieval of warm rain from *CloudSat*. *J. Geophys. Res.*, **116**, D20209, doi:10.1029/2011JD016076.
- , —, D. Vane, G. Stephens, and D. Reinke, 2011: Level 2C RAIN-PROFILE product process description and interface control document algorithm version 0.0. JPL Rep., 14 pp. [Available online at http://www.cloudsat.cira.colostate.edu/sites/default/files/products/files/2C-RAIN-PROFILE-PDICD_P_R04.20110620.pdf.]
- Mace, G. G., Q. Zhang, M. Vaughan, R. Marchand, G. Stephens, C. Trepte, and D. Winker, 2009: A description of hydrometeor layer occurrence statistics derived from the first year of merged *CloudSat* and *CALIPSO* data. *J. Geophys. Res.*, **114**, D00A26, doi:10.1029/2007JD009755.
- Mass, C., 1991: Synoptic frontal analysis: Time for a reassessment? *Bull. Amer. Meteor. Soc.*, **72**, 348–363, doi:10.1175/1520-0477(1991)072<0348:SFATFA>2.0.CO;2.
- , and B. Dotson, 2010: Major extratropical cyclones of the northwest United States: Historical review, climatology, and synoptic environment. *Mon. Wea. Rev.*, **138**, 2499–2527, doi:10.1175/2010MWR3213.1.
- Naud, C. M., A. D. Del Genio, M. Bauer, and W. Kovari, 2010: Cloud vertical distribution across warm and cold fronts in *CloudSat*–*CALIPSO* data and a general circulation model. *J. Climate*, **23**, 3397–3415, doi:10.1175/2010JCLI3282.1.
- , D. J. Posselt, and S. C. van den Heever, 2012: Observational analysis of cloud and precipitation in midlatitude cyclones: Northern versus Southern Hemisphere warm fronts. *J. Climate*, **25**, 5135–5151, doi:10.1175/JCLI-D-11-00569.1.

- , J. F. Booth, and A. D. Del Genio, 2014: Evaluation of ERA-Interim and MERRA cloudiness in the Southern Ocean. *J. Climate*, **27**, 2109–2124, doi:10.1175/JCLI-D-13-00432.1.
- Rienecker, M. M., and Coauthors, 2011: MERRA: NASA's Modern-Era Retrospective Analysis for Research and Applications. *J. Climate*, **24**, 3624–3648, doi:10.1175/JCLI-D-11-00015.1.
- Rudeva, I., and S. K. Gulev, 2011: Composite analysis of North Atlantic extratropical cyclones in NCEP–NCAR reanalysis data. *Mon. Wea. Rev.*, **139**, 1419–1446, doi:10.1175/2010MWR3294.1.
- , and I. Simmonds, 2015: Variability and trends of global atmospheric frontal activity and links with large-scale modes of variability. *J. Climate*, **28**, 3311–3330, doi:10.1175/JCLI-D-14-00458.1.
- Salomonson, V. V., W. L. Barnes, P. W. Maymon, H. E. Montgomery, and H. Ostrow, 1989: MODIS: Advanced facility instrument for studies of the earth as a system. *IEEE Trans. Geosci. Remote Sens.*, **27**, 145–153, doi:10.1109/36.20292.
- Schemm, S., I. Rudeva, and I. Simmonds, 2015: Extratropical fronts in the lower troposphere—Global perspectives obtained from two automated methods. *Quart. J. Roy. Meteor. Soc.*, doi:10.1002/qj.2471, in press.
- Simmonds, I., K. Keay, and J. A. T. Bye, 2012: Identification and climatology of Southern Hemisphere mobile fronts in a modern reanalysis. *J. Climate*, **25**, 1945–1962, doi:10.1175/JCLI-D-11-00100.1.
- Stephens G. L., and Coauthors, 2002: The *CloudSat* mission and the A-Train: A new dimension to space-based observations of clouds and precipitation. *Bull. Amer. Meteor. Soc.*, **83**, 1771–1790, doi:10.1175/BAMS-83-12-1771.
- Stewart, R. E., K. K. Szeto, R. Reinking, S. A. Clough, and S. P. Ballard, 1998: Midlatitude cyclonic cloud systems and their features affecting large scales and climate. *Rev. Geophys.*, **36**, 245–273, doi:10.1029/97RG03573.
- Tselioudis, G., Y. Zhang, and W. B. Rossow, 2000: Cloud and radiation variations associated with northern midlatitude low and high sea level pressure regimes. *J. Climate*, **13**, 312–327, doi:10.1175/1520-0442(2000)013<0312:CARVAW>2.0.CO;2.
- Wang, X. L., Y. Feng, G. P. Compo, V. R. Swail, F. W. Zwiers, R. J. Allan, and P. D. Sardeshmukh, 2013: Trends and low frequency variability of extra-tropical cyclone activity in the ensemble of twentieth century reanalysis. *Climate Dyn.*, **40**, 2775–2800, doi:10.1007/s00382-012-1450-9.
- Wang, Z., D. Vane, G. Stephens, and D. Reinke, 2012: Level 2 combined radar and lidar cloud scenario classification product process description and interface control document. JPL Rep., 22 pp. [Available online at http://www.cloudsat.cira.colostate.edu/sites/default/files/products/files/2B-CLDCLASS-LIDAR_PDICD.P_R04.20120522.pdf.]
- Winker, D. M., M. A. Vaughan, A. H. Omar, Y. Hu, K. A. Powell, Z. Liu, W. H. Hunt, and S. A. Young, 2009: Overview of the *CALIPSO* mission and CALIOP data processing algorithms. *J. Atmos. Oceanic Technol.*, **26**, 2310–2323, doi:10.1175/2009JTECHA1281.1.